Received: 16 November 2017 | Revised: 4 April 2018 | Accepted: 9 May 2018 | Published on: 18 October 2018

DOI: 10.1002/qj.3330

RESEARCH ARTICLE

Quarterly Journal of the Royal Meteorological Society RMetS

Revisiting entrainment relationships for shear-free and sheared convective boundary layers through large-eddy simulations

Cheng Liu[1,2] | Evgeni Fedorovich[2] | Jianping Huang[1]

[1]Yale-NUIST Center on Atmospheric Environment, International Joint Laboratory on Climate and Environment Change (ILCEC), Nanjing University of Information Science and Technology, Nanjing, China
[2]School of Meteorology, University of Oklahoma, Norman, Oklahoma

Correspondence
Evgeni Fedorovich, 120 David L. Boren Blvd, NWC/SoM, University of Oklahoma, Norman, OK 73072, USA.
Email: fedorovich@ou.edu

Funding information
National Natural Science Foundation of China, 41575009, Grant 41575009. Postgraduate Research and Practice Innovation Program of Jiangsu Province, KYLX16_0945, Grant KYLX16_0945. Priority Academic Program Development of Jiangsu Higher Education Institutions, PAPD. Ministry of Education of China, PCSIRT. Priority Academic Program Development of Jiangsu Higher Education Institutions (PAPD). National Key Research and Development Program of China, 2017YFC0210102.

Entrainment is critical to the development of the atmospheric convective boundary layers (CBLs) and for the exchange of energy and substances between the boundary layer and free atmosphere. In this study, entrainment relationships are systematically evaluated from large-eddy simulations (LESs) of shear-free and sheared CBLs under a broad variety of atmospheric conditions. A total of 36 LES runs are conducted for varying free-atmosphere stratifications, surface heat fluxes, and height-constant geostrophic winds. It has been found that entrainment flux ratios have a common value of 0.2 regardless of the stratification of free atmosphere and the surface heat-flux value when analysed within the zero-order-model (ZOM) framework for the shear-free CBLs, whereas the actual (LES) entrainment ratios are not only stratification-dependent, but also surface heat flux-dependent. For the sheared CBLs, the entrainment-flux ratios are substantially increased when the geostrophic winds are strong while they have a slight reduction under weak wind conditions. In the free-encroachment regime, the dimensionless entrainment rates have been found to be approximately constant and surface heat-flux independent, with the value in the range from 0.4 to 0.7 depending on the method used to evaluate the CBL depth.

KEYWORDS
convective boundary layer, entrainment ratio, entrainment relationships, free encroachment, thermal stratification, wind shear

1 | INTRODUCTION

The clear atmospheric convective boundary layer (CBL), driven primarily by the heat (buoyancy) transfer from the warm underlying surface and secondarily affected by wind shears, is commonly observed in the atmosphere during fair weather daytime conditions (Stull, 1998; Holtslag and Duynkerke, 1998; Fedorovich *et al.*, 2004). In the presence of wind shear, the layer is referred to as sheared CBL, and is called shear-free (or shearless) CBL when the shear effect is absent or negligible in comparison with the buoyancy contribution. The CBL is typically much more turbulent than the main portion of the troposphere within which it develops. The CBL air is vertically well mixed due to the vigorous turbulent motions resulting from the buoyant turbulence production and the shear-generated turbulence. Due to this mixing, the CBL is often called the convectively mixed layer.

Most commonly, the CBL develops through the process of convective entrainment – a continual turbulent exchange of air and transported atmospheric substances between the CBL and the quiescent free-atmospheric region aloft. Since the free atmosphere is typically stably stratified and has its (virtual) potential temperature increasing with height, it represents the heat source for the CBL, and the warmer, more buoyant air from the troposphere is transported downward into the mixed layer as a result of entrainment. The entrainment layer (zone) thus acts as an interface between the mixed core of the CBL and the free atmosphere. Because the (virtual) potential temperature grows so sharply throughout the entrainment layer that the corresponding absolute

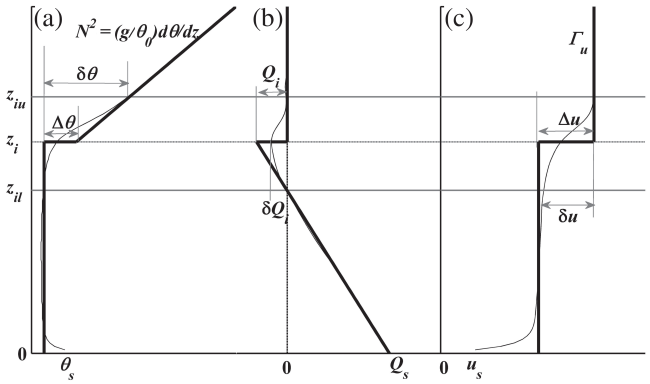

FIGURE 1 Sketch of (a) potential temperature, (b) kinematic heat (potential temperature) flux, and (c) *x*-component of wind in the horizontally homogeneous CBL. Thin black lines indicate actual (LES) profiles, and black bold lines present their ZOM counterparts. Grey horizontal lines indicate the lower, z_{il}, and upper, z_{iu}, limits of the entrainment zone

air temperature increment across the layer is often positive, the entrainment layer is called also the capping inversion layer or simply capping inversion. Convective entrainment is a key process that determines the vertical redistribution of heat, momentum and scalars in the lower atmosphere during daytime. The entrainment happens on scales of motion that are typically not resolved by meso- and larger-scale atmospheric models, so the entrainment effects in such models need to be parametrized. Usually such parametrizations are constructed in terms of the so-called integral parameters of entrainment (Fedorovich *et al.*, 2004). Among the basic entrainment parameters considered are the capping-inversion (entrainment-zone) thickness, the entrainment rate dz_i/dt, that is the rate of change in time of inversion height z_i in the absence of large-scale subsidence (here z_i is commonly defined as the level of the heat-flux minimum within the entrainment zone), and the entrainment (flux) ratios for various entrained substances. For heat, the entrainment ratio is given by $A_i = -\delta Q_i/Q_s$, where δQ_i is the kinematic flux of heat at z_i (the entrainment heat flux; note that this flux is directed downwards, so it is negative), and $Q_s \geq 0$ is the surface heat flux (see schematic in Figure 1). In the entrainment parametrizations developed for atmospheric models, the integral parameters are usually sought as functions of the free-atmosphere stratification, typically assumed to be linear and continuous, and surface fluxes of heat, momentum and scalars. Historically, many parametrizations of this kind have been proposed and discussed in the literature (e.g. Lilly, 1968; Betts, 1973; 1974; Carson, 1973; Stull, 1973; Tennekes, 1973; Zeman and Tennekes, 1977; Deardorff, 1979; Driedonks, 1982; Driedonks and Tennekes, 1984; Zilitinkevich, 1991; Fedorovich, 1995; 1998; Fedorovich and Mironov, 1995; Fedorovich *et al.*, 2004; Conzemius and Fedorovich, 2006b; 2007; Pino *et al.*, 2006; Kim *et al.*, 2006; Sun and Wang, 2008; Garcia and Mellado, 2014).

Most of these parametrizations have been proposed and tested using the so-called bulk models of entrainment of different degrees of complexity. The first of such models, the zero-order jump bulk model (ZOM) was originally proposed by Lilly (1968) for the shear-free CBL entrainment. In the ZOM, the entrainment zone is considered, in a horizontally average sense, as a zero-order discontinuity interface which is propagating upwards in time. Across this interface, the meteorological variables, averaged over horizontal planes, change in a jump-like manner. In the ZOM, the entrainment heat flux is given by $Q_i = -\Delta\theta(dz_i/dt)$, where $\Delta\theta$ is the (virtual) potential temperature jump across the zero-order interface at z_i (Zilitinkevich, 1991); see Figure 1. The ZOM approach was later generalized also for the sheared CBL (e.g. Fedorovich, 1995; Conzemius and Fedorovich, 2006b). Details of entrainment parametrizations developed within the ZOM framework are presented in the next sections of our article. According to methodology adopted in our study, the smoothed profiles of potential temperature and wind velocity, which are approximated using the ZOM assumptions, are retrieved from observations or numerical simulations by horizontal averaging in a fixed coordinate system. As discussed in Lilly (2002), the actual interface between the mixed-layer and free-atmosphere air is rather convoluted, so if a coordinate transformation is applied by normalizing the vertical coordinate by the local interface height, with horizontal averaging being performed in the normalized coordinate system, the averaged profiles would retain the sharpness of the interface.

Following the ZOM, higher-order bulk models of convective entrainment have been developed that allowed for a finite inversion-layer thickness. Performance of the first-order model of entrainment with linear potential temperature profile across the capping inversion, originally proposed by Betts (1974), was studied in Van Zanten *et al.* (1999), Conzemius and Fedorovich (2006b; 2007), Pino *et al.* (2006), Kim *et al.* (2006), and Sun and Wang (2008) using large-eddy simulation (LES) data. A higher-order general-structure model of entrainment originally outlined in Deardorff (1979) was further advanced in Fedorovich and Mironov (1995), who employed a self-similar representation of the potential temperature profile within the entrainment zone. The model was tested against LES data in Fedorovich *et al.* (2004). Both first-order and general-structure approaches found only limited applicability in the atmospheric modelling due to their relative complexity, where ZOM-based parametrizations of entrainment were used rather extensively, primarily because of their simplicity and practicality.

Relationships between the integral parameters of the shear-free entrainment resulting from ZOM were thoroughly evaluated through LES in Fedorovich *et al.* (2004). One of the goals of that study, focused on the convective entrainment in a linearly stratified atmosphere, was to compare the ZOM-parametrized entrainment characteristics with their counterparts directly retrieved from the LES output. The particular emphasis was placed on the entrainment relationships in the so-called equilibrium regime, where the entrainment buoyancy flux remains in an approximate steady balance with

the surface buoyancy flux and the integral of the turbulence kinetic energy (TKE) dissipation rate throughout the CBL, which makes the rate of change of CBL-averaged TKE negligibly small. Data from other numerical and experimental studies were also used in the analysis. The investigated ranges of the CBL depth and the stratification strength in the free atmosphere covered most of their natural variability. Importantly, it was found that entrainment parameters essentially depend on the model framework chosen for interpretation of the LES data. Particularly, the entrainment ratio retrieved within a conceptual framework of ZOM showed a universal value of about 0.2 for a broad range of the Brunt–Väisälä frequency N adopted as a measure of stratification strength in the free atmosphere. It agrees with the estimate of Stull (1976), who suggests A_i equal to 0.2 after reviewing several observational studies, and with the findings of laboratory tank experiments (Deardorff *et al.*, 1980). On the contrary, the entrainment ratio A_i directly evaluated from the entrainment heat flux predicted by LES at the CBL top demonstrated strong dependence on N, showing A_i value approaching the ZOM estimate $\Delta\theta(dz_i/dt)/Q_s \approx 0.2$ with increasing N, thus supporting the results of Sorbjan (1996). However, numerical simulations in the studies of Sorbjan (1996) and Fedorovich *et al.* (2004) were all run with the same surface heat flux Q_s, and, to our best knowledge, discrepancies between the actual and ZOM entrainment ratios with respect to variation of the surface heat flux have not been investigated. We fill this gap and investigate these discrepancies in the study to be reported in the present article.

In the sheared CBL, the entrainment process is additionally affected by flow (wind) shears that are primarily concentrated in the near-surface region of the flow and within the entrainment zone (Fedorovich and Conzemius, 2008). Several observational studies have reported much higher A_i values on the order of 0.5 (Betts and Ball, 1994; Barr and Strong, 1996; Angevine, 1999), which could be attributed to the shear contribution. It was also shown in the LES studies of Moeng and Sullivan (1994), Kim *et al.* (2003), Pino *et al.* (2003), Conzemius and Fedorovich (2006a; 2006b) and Pino and Vilà-Guerau de Arellano (2008) that the entrainment ratio for heat, A_i, generally increases in the presence of wind shear, no matter how the shear is vertically distributed throughout the CBL. However, aforementioned studies either considered only one factor affecting the entrainment or did not directly focus on the ratio in their analysis. As was noted in Conzemius and Fedorovich (2006a), under particular combinations of the surface flux and free-atmosphere stratification strength, the imposed shear may lead to attenuation of the entrainment. However, it would be hard to conclude from the above-mentioned studies how the variation of wind shear across the CBL would modify the entrainment ratio, as all these studies were conducted with different simulation set-ups and focusing on effects of different external forcings. Thus, a systematic investigation of the progressively growing across-CBL wind shear on the entrainment ratio would be warranted. Such an investigation is another part of the reported study.

Another aspect of the CBL entrainment that has not been systematically studied is associated with the limiting value of the entrainment rate in the regime of so-called free encroachment (also called the free entrainment in some earlier works), when the CBL is growing in the neutrally stratified atmosphere with $N = 0$ and with zero entrainment heat flux (hence, encroachment instead of entrainment; although the word entrainment is kept in the names of some parameters used to describe this regime). The growth of CBL by free encroachment was studied in laboratory experiments by Deardorff (1974) and Deardorff *et al.* (1980), and by means of numerical simulations in Sorbjan (1996) and Mellado (2012). These studies obtained rather varying estimates for the free-encroachment value of the dimensionless entrainment rate $E = {w_*}^{-1}(dz_i/dt)$, where $w_* = [(g/\theta_0)z_i Q_s]^{1/3}$ is the Deardorff convective velocity scale, g is acceleration due to gravity, and θ_0 is a constant reference temperature value (300 K in this study). All these studies were conducted with the shear-free CBL. According to the analysis of Zilitinkevich (1991), E should tend to a constant value in the free-encroachment regime. In the atmosphere, the closest analogue of this regime is observed in the late morning, when the CBL is growing through the remnants of the neutrally (or almost neutrally) stratified residual layer from the previous day. To shed some extra light on the free-encroachment CBL growth and check universality of the corresponding dimensionless growth rate, we conducted a series of LES experiments with a CBL propagating in a neutrally stratified environment and driven by different values of the surface heat flux.

In our study, LES has been employed to investigate several remaining aspects of convective entrainment that were insufficiently or incompletely investigated in the previous studies. The investigation is focused on the behaviour of the entrainment rate and entrainment ratio under a variety of forcing conditions in a dry CBL. Specific questions addressed in the study are the following:

1. How much does the entrainment heat flux ratio directly predicted by LES depend on the surface heat flux as compared to the entrainment ratio retrieved from LES using the ZOM formalism?
2. How does magnitude of wind shear across the CBL affect the heat entrainment ratio?
3. How does the entrainment rate change with varying surface heat flux under the free-encroachment conditions?

The article is organized as follows. First, in section 2, we briefly introduce the ZOM of entraining CBL and describe how it is used to retrieve entrainment parameters from output of the employed LES, whose basic set-up features are also outlined in the section. Then we address questions (1), (2) and (3), and offer answers to them in the correspondingly

numbered subsections of section 3. Section 4 contains summary and conclusions.

2 | METHODS

2.1 | Zero-order model of entrainment

The ZOM of CBL has been broadly used to facilitate our understanding of the dynamic and thermodynamic processes of CBL since it was originally proposed by Lilly (1968). Figure 1 illustrates representation of the CBL structure according to the ZOM. Spatially (over the horizontal plane) averaged meteorological fields within CBL are constant with height in the ZOM. The entrainment zone (capping inversion layer) is represented by a discontinuity interface, across which the averaged potential temperature θ and wind velocity u (without loss of generality we may consider only one component of it) experience zero-order jumps $\Delta\theta$ and Δu, respectively. Above the CBL, in the free atmosphere, the ZOM potential temperature is steady and has a positive vertical gradient $d\theta/dz$ that may be expressed in terms of height- and time-constant Brunt–Väisälä frequency $N = \sqrt{(g/\theta_0)(d\theta/dz)}$, so that $d\theta/dz = N^2\theta_0/g = const$. The free-atmosphere vertical gradient of u was assumed to be zero in our study. In the ZOM, the heat flux drops linearly from the surface value Q_s to $Q_i = -\Delta\theta(dz_i/dt)$ at z_i (Zilitinkevich, 1991). Similar considerations apply to the ZOM wind velocity profile and momentum flux profile (Fedorovich, 1995).

Vertical integration of the horizontally averaged heat-balance equation $\partial\theta/\partial t = -\partial Q/\partial z$ from the surface to the CBL top, considering the ZOM profiles shown in Figure 1, where Q is the kinematic heat flux, provides the ZOM integral heat budget in the form (Zilitinkevich, 1991; Fedorovich, 1995; Fedorovich *et al.*, 2004):

$$\frac{d}{dt}\left(\frac{N^2 {z_i}^2}{2} - z_i \Delta b\right) = B_s, \tag{1}$$

where b is the buoyancy defined through $b = (g/\theta_0)(\theta - \theta_0)$, and $\Delta b = (g/\theta_0)\Delta\theta$ is the buoyancy increment across the discontinuity interface at z_i defined as the level of the heat-flux minimum at the CBL top, and $B_s = (g/\theta_0)Q_s$ is the surface buoyancy flux. To obtain Equation 1, we take into account that in ZOM there is no flux of heat at the upper side of the discontinuity interface and that free-atmosphere potential temperature at this side of the interface is given by $\theta_{g0} + (d\theta/dz)z_i$, where θ_{g0} is the temperature that the free-atmosphere potential temperature reaches being extrapolated to the ground level ($z = 0$); see Fedorovich (1995).

Note that the ZOM approximation of the CBL structure differs in several important aspects from the realistic CBL structure, elements of which are presented in Figure 1 by thin curved lines (these lines represent a particular realization of the horizontally averaged LES solution). For instance, the ZOM temperature increment $\Delta\theta$ across the entrainment zone (reduced to the zero-thickness interface) is rather different from the potential temperature jump $\delta\theta$ across the realistic entrainment layer located in Figure 1 between the lower, z_{il}, and upper, z_{iu}, interfaces of the region with negative heat flux of entrainment. Correspondingly, the realistic value δQ_i of the heat flux of entrainment in its minimum at z_i located between z_{il} and z_{iu} is different from the ZOM value $Q_i = -\Delta\theta(dz_i/dt)$ at z_i. The procedure of retrieval of the ZOM temperature (buoyancy) and wind profiles from LES output data is described in section 2.3, following Fedorovich *et al.* (2004) and Conzemius and Fedorovich (2006a).

Another important ZOM equation, the integral TKE budget equation (it may also be interpreted as the ZOM entrainment equation), is obtained – as explained in Zilitinkevich (1991) – by vertically integrating the TKE balance equation from the surface to the CBL top with using the ZOM representation of the CBL structure and assuming that TKE is well mixed within the CBL, so that there is no TKE above the upper side of the ZOM discontinuity interface. In connection with the ZOM application to the shear-free CBL developing into a linearly stratified atmosphere, Fedorovich *et al.* (2004) considered the truncated version of the ZOM entrainment equation pertinent to the so-called equilibrium entrainment regime, in which

$$\frac{\Delta b(dz_i/dt)}{B_s} = C_1, \tag{2}$$

where C_1 is a universal constant representing the ZOM fraction of buoyancy-produced TKE consumed for entrainment in the shear-free CBL. When written in dimensionless form by using N and B_s as scaling parameters, Equations 1 and 2 transform into

$$\frac{d}{d\hat{t}}\left(\frac{\hat{z}_i^2}{2} - \hat{z}_i \Delta\hat{b}\right) = 1, \tag{3}$$

$$\Delta\hat{b}\frac{d\hat{z}_i}{d\hat{t}} = C_1, \tag{4}$$

where $\hat{z}_i = z_i {B_s}^{-1/2} N^{3/2}$, $\Delta\hat{b} = \Delta b {B_s}^{-1/2} N^{-1/2}$, and $\hat{t} = tN$ are the normalized CBL depth, ZOM buoyancy increment, and time, respectively. The normalized equations have the following analytical solutions (Zilitinkevich, 1991; Fedorovich *et al.*, 2004):

$$\hat{z}_i = [2(1 + 2C_1)\hat{t}]^{1/2}, \tag{5}$$

$$\Delta\hat{b} = C_1[2\hat{t}/(1 + 2C_1)]^{1/2}. \tag{6}$$

The above solutions indicate that in the equilibrium entrainment regime, the normalized CBL depth and buoyancy (or potential temperature) increment defined in ZOM terms are expected to be universal 1/2-power-law functions of the dimensionless time. Equation (2), on the other hand, shows that ZOM shear-free entrainment heat ratio $A = -Q_i/Q_s = \Delta\theta(dz_i/dt)/Q_s$ under the equilibrium entrainment conditions should have the universal constant value C_1, so the equilibrium heat entrainment ratio should be independent of time, external stratification, and surface heat flux. The dimensionless entrainment rate $E = {w_*}^{-1}(dz_i/dt)$ in the

TABLE 1 Settings for surface heat flux and potential-temperature gradient in the free atmosphere. qFnG is the case name (q is the surface heat-flux identifier, F is the heat-flux case number, n is the identifier of the potential-temperature gradient in the free atmosphere, and G is the temperature-gradient case number); 0, 5, 10, 20 are magnitudes of geostrophic wind in m/s. N value is 0.0057 s^{-1}, 0.0099 s^{-1}, and 0.0181 s^{-1}, respectively, corresponding to the potential temperature gradient of 0.001, 0.003, and 0.01 K/m

		Surface heat flux Q_s (K m s^{-1})		
	n\q	**0.03**	**0.1**	**0.3**
Potential temperature gradient $d\theta/dz$ (K/m)	0.001	q1n1(0, 5, 10, 20)	q2n1(0, 5, 10, 20)	q3n1(0, 5, 10, 20)
	0.003	q1n2(0, 5, 10, 20)	q2n2(0, 5, 10, 20)	q3n2(0, 5, 10, 20)
	0.01	q1n3(0, 5, 10, 20)	q2n3(0, 5, 10, 20)	q3n3(0, 5, 10, 20)

regime of the equilibrium shear-free entrainment is given by (Fedorovich *et al.*, 2004):

$$E = \hat{z}_i^{-1/3}\frac{d\hat{z}_i}{d\hat{t}} = \frac{1}{2}[2(1+2C_1)]^{1/3}\hat{t}^{-2/3}. \quad (7)$$

The existence of the equilibrium entrainment regime in a shear-free CBL was confirmed in LES experiments of Fedorovich *et al.* (2004), who demonstrated (see their Figure 3) that LES solutions for $\hat{z}_i$ with different N values converge at sufficiently large $\hat{t}$ to a single power-law line represented by Equation 5 with $C_1 \sim 0.2$. However, the convergence of $\hat{z}_i$ was not investigated for varying B_s, nor were the equilibrium entrainment predictions for $\Delta\hat{b}$ and E, (6) and (7), verified with different N and B_s.

2.2 | Large-eddy simulation of entrainment

The LES code employed in this study was originally developed by Moeng (1984) and later refined by Sullivan *et al.* (1996), Patton *et al.* (2005), and Huang *et al.* (2008; 2009; 2011). In the code, the no-slip and impermeability conditions are used for velocity field at the surface, and the spatially uniform surface heat flux is prescribed. Monin–Obukhov similarity theory is employed for the formulation of the bottom boundary conditions (Sullivan *et al.*, 1994), and the subgrid turbulent transport is modelled following Deardorff's (1980) approach based on the parametrized prognostic equation for subgrid TKE. A radiation boundary condition (Klemp and Durran, 1983) is applied at the top to reduce the impact of gravity waves in the upper portion of the computational domain. In the horizontal directions, periodic boundary conditions are used. The third-order Runge–Kutta scheme is employed for advancement of all prognostic fields in time. The pressure is obtained diagnostically from the Poisson solver. The surface roughness length for momentum in the reported simulations is set equal to 0.1 m.

The standard domain size of our simulation was 5 km × 5 km × 2 km, with grid spacing of 50 m × 50 m × 20 m in the x, y and z directions, respectively. A larger domain of 10 km × 10 km × 4 km with finer grid spacing of 25 m × 25 m × 10 m was employed to test the effects of grid spacing on the solutions. Test results show that the mean turbulence statistics from two simulations have a difference less than 8%, and the solutions for entrainment parameters obtained with these two domains are insensitive to the grid spacing.

A series of numerical experiments are designed to examine the impacts of surface heat fluxes, free-atmosphere stratifications, and wind shears on entrainment integral parameters. As listed in Table 1, values of the surface kinematic heat flux, 0.03, 0.1 and 0.3 K m s^{-1}, and free-atmosphere potential-temperature gradient, 0.001, 0.003 and 0.01 K/m, are varied within ranges similar to the ranges adopted in Conzemius and Fedorovich (2006a). To study effects of wind shear on the entrainment parameters, all CBL simulation cases have been run with four different geostrophic winds aligned with the x-axis and having magnitudes of 0, 5, 10 and 20 m/s. Thus, a total of 36 simulations are completed in this study. For each scenario run, potential temperature θ has the initial vertical profile with a constant increasing rate throughout the simulation domain. The Coriolis parameter f in the simulations is set to a midlatitude constant value of 10^{-4} s^{-1}.

2.3 | Evaluation of entrainment parameters from the LES output

As demonstrated in Figure 1 and discussed in section 2.1, average profiles of meteorological variables and associated entrainment parameters in the ZOM differ from their actual CBL counterparts. In our study, the role of actual data has been played by the mean-flow profiles and turbulent fluxes retrieved from the LES output by spatial averaging over the horizontal planes and complementary averaging in time, with the averaging intervals chosen depending on the CBL growth rate, which differed between the simulated cases (e.g. every 100 time steps for q3n1, 200 time steps for q1n1, q2n1, q2n2, q3n2, q3n3, and 1,000 time steps for q1n2, q1n3, q2n3). All simulations have been run long enough to achieve the quasi-equilibrium regime of entrainment that has been verified through the approximate stationarity of the mean TKE within the CBL. As explained in Fedorovich *et al.* (2004) and Conzemius and Fedorovich (2006a), the ZOM profiles should be derived from the LES in a manner consistent with their definition. For example, one may come to wrong conclusions regarding the entrainment properties by taking $\delta\theta$ instead of $\Delta\theta$ or interpreting Q_i as δQ_i (Fedorovich *et al.*, 2004).

Keeping the ZOM representation of the CBL structure in mind, the CBL inversion height z_i (interpreted at the CBL top in the ZOM) has been defined in our study as the level of the LES-derived heat-flux minimum within the entrainment zone. The ZOM temperature increment $\Delta\theta$ is calculated as the difference between the potential temperature value at z_i obtained by extrapolation of the free-atmosphere temperature profile to level z_i and the mean (i.e. height-averaged beneath z_i) temperature in the mixed layer. The same method has been applied to calculate Δu. The ZOM entrainment heat flux was evaluated as $Q_i = -\Delta\theta(dz_i/dt)$. The actual heat flux δQ_i of entrainment at z_i and actual potential temperature increment $\delta\theta$ across the entrainment zone were evaluated from the corresponding LES profiles as illustrated in Figure 1.

3 | RESULTS

3.1 | Shear-free entrainment

In order to answer the first question posed in section 1, that is how much does the entrainment heat flux ratio directly predicted by LES depend on the surface heat flux as compared to the entrainment ratio retrieved from LES using the ZOM formalism, we start our analysis with examination of the simulated CBL cases without wind shear. Although we show the data covering the whole simulation period, we present our interpretations regarding the entrainment parameter behaviour for only the quasi-equilibrium regime. As indicated in section 2.1, one would expect normalized z_i and Δb, deduced from the LES outputs using the ZOM approximation, to behave in the equilibrium entrainment regime as predicted by (5) and (6). We compare LES-estimated $\hat{z}_i = z_i B_s^{-1/2} N^{3/2}$ and $\Delta\hat{b} = \Delta b B_s^{-1/2} N^{-1/2}$ with these equilibrium ZOM solutions in Figure 2a,b. At the same time, we also provide the actual values of these variables in Table 2. At large $\hat{t}$, the normalized CBL depth $\hat{z}_i$ calculated from LES shows excellent agreement with the equilibrium ZOM solution (5) for $C_1 = 0.2$ irrespective of the values of surface heat flux and the free-atmosphere buoyancy frequency used for normalization. Fedorovich *et al.* (2004) have previously demonstrated the validity of relationship (5) for different values of N, with $C_1 = 0.17$ that is fairly close to 0.2. Here, we find out that this relationship also works for different surface heat flux values within a range of its typical natural variability. The normalized buoyancy increment Δb, whose evaluation from LES data is less accurate than that of z_i, follows Equation 6 with $C_1 = 0.2$ rather closely as well, although showing some degree of scattering. The same can be said about the dimensionless entrainment rate (Figure 2c), which confidently follows the $-2/3$ power-law prediction Equation 7, again with $C_1 = 0.2$. Since parameter C_1 in the ZOM of CBL has also a meaning of the heat entrainment ratio, from our LES results we may conclude that the ZOM equilibrium entrainment ratio in a shear-free CBL is fairly constant under typical surface heat flux and free-atmosphere stratification conditions and has a value close to 0.2 (Zilitinkevich, 1991).

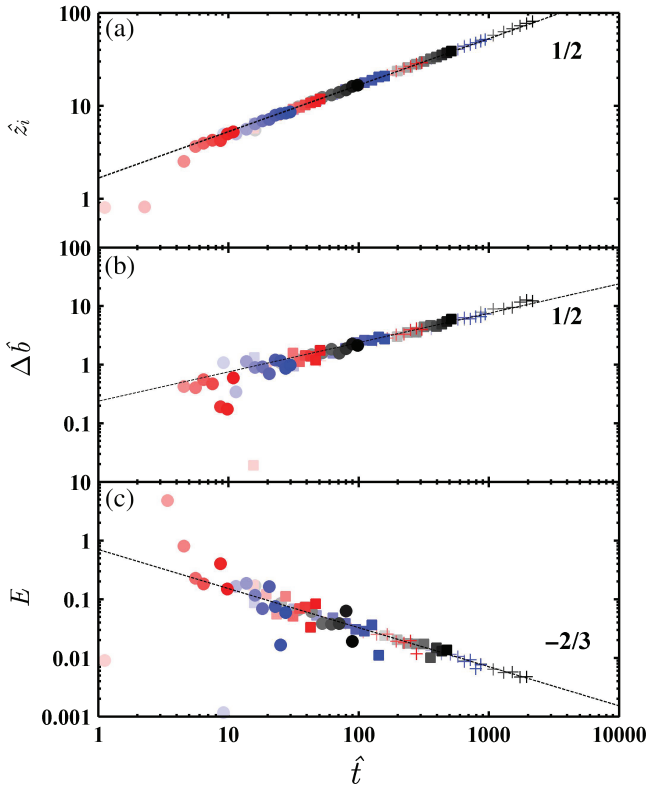

FIGURE 2 Dimensionless CBL parameters as functions of dimensionless time in log coordinates: (a) normalized CBL depth; (b) normalized buoyancy increment across the inversion layer; (c) dimensionless entrainment rate. The dashed straight line indicates corresponding universal ZOM solutions with $C_1 = 0.2$ for shear-free CBL: (a) $\hat{z}_i = [2(1 + 2C_1)\hat{t}]^{1/2}$, (b) $\Delta\hat{b} = C_1[2\hat{t}/(1 + 2C_1)]^{1/2}$; and (c) $E = \frac{1}{2}[2(1 + 2C_1)]^{1/3}\hat{t}^{-2/3}$. The light colour of symbols indicates early times, while dark colours represent later times. Different symbol shapes correspond to different values of the background potential temperature gradient: circle, $d\theta/dz = 0.001$ K/m; square, $d\theta/dz = 0.003$ K/m; cross, $d\theta/dz = 0.01$ K/m. Different symbol colours correspond to different surface heat-flux values: black, $Q_s = 0.03$ K m s^{-1}; blue, $Q_s = 0.1$ K m s^{-1}; red, $Q_s = 0.3$ K m s^{-1} [Colour figure can be viewed at wileyonlinelibrary.com].

The above result, however, applies only to the ZOM entrainment ratio $A = \Delta\theta(dz_i/dt)/Q_s = C_1$, while the actual ratio of the negative heat flux of entrainment δQ_i to the surface heat flux Q_s neither has reasons to remain constant under changing Q_s and N, nor needs its value to be associated with C_1, which is entirely a ZOM quantity. In Figure 3, we compare the actual (LES) entrainment flux ratio (evaluated as $A_i = -\delta Q_i/Q_s$; see Figure 1) with the ZOM entrainment flux ratio $A = 0.2$ for all nine simulated shear-free CBL cases. It is clear from the presented data that the actual ratio $A_i = -\delta Q_i/Q_s$ is highly dependent on Q_s and N. Some general tendencies become apparent from the close inspection of individual plots in Figure 3. First, one can easily see that at given Q_s the actual entrainment ratio increases with N, getting closer to the ZOM 0.2 value. This behaviour has been analysed and explained in Fedorovich *et al.* (2004), who attributed it to the change of shape of the heat-flux profile in the lower portion of the

TABLE 2 The actual time (t), CBL depth (z_i), and potential temperature jump ($\Delta\theta$) for all data points shown in Figure 2. Dashes indicate cases when the evaluation of the corresponding parameter was impossible

		1	2	3	4	5	6	7	8	9	10
q1n1	t(s)	2,796	4,396	5,996	7,596	9,196	10,796	12,396	13,996	15,596	17,196
	z_i (m)	398	597	710	804	895	954	1,013	1,074	1,177	1,209
	$\Delta\theta$(K)	-	0.08	0.09	0.11	0.12	0.13	0.11	0.14	0.16	0.16
q1n2	t(s)	15,996	19,996	23,996	27,996	31,996	35,996	39,996	43,996	47,996	51,996
	z_i (m)	667	750	823	888	954	1,021	1,061	1,121	1,175	1,232
	$\Delta\theta$(K)	0.26	0.29	0.34	0.34	0.42	0.45	0.43	0.47	0.52	0.57
q1n3	t(s)	11,996	23,996	35,996	47,996	59,996	71,996	83,996	95,996	107,996	119,996
	z_i (m)	316	463	569	657	739	807	869	934	989	1,046
	$\Delta\theta$(K)	0.45	0.66	0.76	1.01	1.15	1.16	1.21	1.50	1.62	1.58
q2n1	t(s)	1,596	1996	2,396	2,796	3,196	3,596	3,996	4,396	4,796	5,196
	z_i (m)	659	660	746	846	912	951	1,048	1,093	1,103	1,139
	$\Delta\theta$(K)	0.14	0.05	0.15	0.12	0.12	0.09	0.16	0.15	0.11	0.13
q2n2	t(s)	1,596	3,196	4,796	6,396	7,996	9,596	11,196	12,796	14,396	15,996
	z_i (m)	376	525	656	765	869	956	1,028	1,096	1,185	1,213
	$\Delta\theta$(K)	0.23	0.16	0.25	0.27	0.33	0.41	0.45	0.45	0.52	0.48
q2n3	t(s)	15,996	19,996	23,996	27,996	31,996	35,996	39,996	43,996	47,996	51,996
	z_i (m)	668	751	823	890	956	1,017	1,069	1,125	1,165	1,213
	$\Delta\theta$(K)	0.87	0.96	1.12	1.34	1.40	1.50	1.43	1.57	1.54	1.73
q3n1	t(s)	196	396	596	796	976	1,125	1,317	1,519	1,714	1900
	z_i (m)	185	188	20	582	842	911	984	973	1,141	1,203
	$\Delta\theta$(K)	-	-	-	0.10	0.09	0.13	0.11	0.04	0.04	0.14
q3n2	t(s)	1,571	1971	2,369	2,769	3,164	3,547	3,936	4,316	4,712	5,105
	z_i (m)	579	702	793	837	926	966	1,024	1,084	1,112	1,185
	$\Delta\theta$(K)	0.01	0.26	0.35	0.30	0.48	0.34	0.43	0.42	0.36	0.53
q3n3	t(s)	2,796	4,396	5,996	7,595	9,186	10,786	12,352	13,876	15,409	16,896
	z_i (m)	470	604	715	799	878	961	1,025	1,084	1,149	1,189
	$\Delta\theta$(K)	0.47	0.75	1.04	1.06	1.16	1.33	1.34	1.59	1.69	1.63

entrainment zone with growing N. With stratification getting stronger, the negative flux of entrainment gets restrained to a shallower region below z_i, with very little entrainment taking place above the z_i level, and the overall shape of the actual heat flux profile between z_{il} and z_i becomes closer to the linear ZOM profile shape, thus leading to larger values of $-\delta Q_i$. Secondly, the plots in Figure 3 show that increasing Q_s at given N results in the progressively smaller entrainment-ratio values. We know of no existing interpretations of this effect, but suggest that it can be again explained in terms of the actual Q profile shape change within the entrainment zone at different Q_s. With fixed N, the penetrability of convective motions into the stably stratified fluid aloft is determined by their integral kinetic energy proportional to ${w_*}^2 \propto {Q_s}^{2/3}$, so one would expect the penetration distance, which is roughly proportional to the depth of the entrainment zone, to grow with Q_s. On the other hand, with smaller Q_s the actual heat-flux profile in the entrainment zone will be more vertically constrained and have a shape closer to that of the ZOM entrainment-zone heat-flux profile. Visual estimates of the Q profile shapes at different Q_s (not shown) generally support this explanation. In summary, our LES data indicate that actual entrainment ratio $A_i = -\delta Q_i/Q_s$ reaches its maximum value in the CBL case with strongest free-atmosphere stratification and weakest surface heat flux. Results presented in Figures 2 and 3 provide the answer to our question (1): while the entrainment flux ratio according to ZOM, $\Delta\theta(dz_i/dt)/Q_s$, has a common value of 0.2 regardless of the free-atmosphere stratification and surface heat flux, the actual entrainment ratio $-\delta Q_i/Q_s$ is notably stratification- and heat-flux dependent; it increases with growing N and decreases with growing Q_s.

3.2 | Sheared entrainment

Sheared CBLs are organized in a more complicated manner than shear-free CBLs (Gibbs and Fedorovich, 2014; Salesky *et al.*, 2017). The generally accepted knowledge regarding the influence of wind shear on the convective entrainment is that shear intensifies the entrainment and enhances the CBL growth, e.g. LES data in Conzemius and Fedorovich (2006a; 2006b) and observational studies reviewed in Fedorovich and Conzemius (2008). However, this knowledge is mostly coming from studies, where the wind shear magnitude was not systematically varied within its representative atmospheric range of values.

Figure 4 presents the normalized CBL depth as a function of dimensionless time under different geostrophic winds aligned with the x-axis. We kept the same scaling for z_i

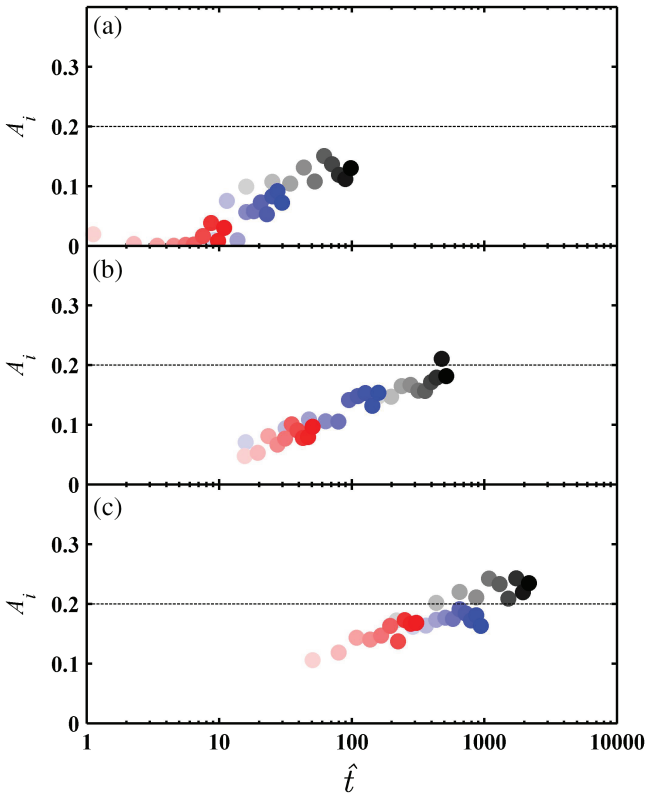

FIGURE 3 Entrainment flux ratio A_i as function of dimensionless time for different stratifications in the free atmosphere: (a) $d\theta/dz = 0.001$ K/m, (b) $d\theta/dz = 0.003$ K/m, and (c) $d\theta/dz = 0.01$ K/m. Symbols show LES data stratified over time: light colours indicate early times and dark colours indicate later times. The dashed straight lines indicate the entrainment ratio according to the universal ZOM solution. Different colours correspond to different values of Q_s: black, $Q_s = 0.03$ K m s^{-1}; blue, $Q_s = 0.1$ K m s^{-1}; red, $Q_s = 0.3$ K m s^{-1} [Colour figure can be viewed at wileyonlinelibrary.com].

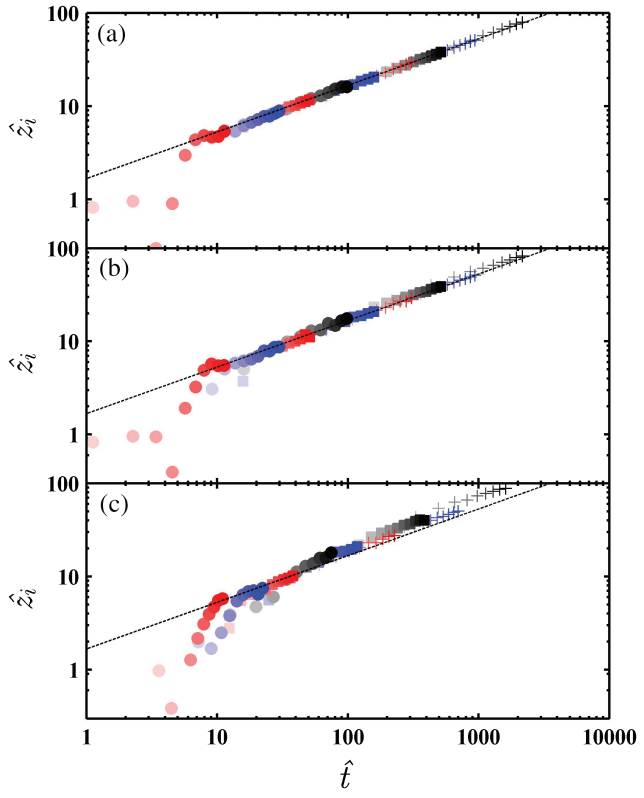

FIGURE 4 Dimensionless CBL depth as function of dimensionless time for different geostrophic-wind magnitudes: (a) $u_g = 5$ m/s, (b) $u_g = 10$ m/s, and (c) $u_g = 20$ m/s. The colours and symbols have the same meanings as in Figure 2 [Colour figure can be viewed at wileyonlinelibrary.com].

and t as in Figure 2a in order to single out the wind shear effects on z_i dynamics in comparison with the shear-free conditions. With relatively weak geostrophic wind, 5 m/s (Figure 4a), $\hat{z}_i$ appears to follow very closely the ZOM theoretical prediction for shear-free CBL (Figure 2a). However, with geostrophic wind increasing to 10 m/s (Figure 4b), $\hat{z}_i$ starts showing departure toward higher values (especially noticeable at large $\hat{t}$), thus pointing to the faster CBL growth in the presence of shear. This departure becomes more apparent when geostrophic wind increases to 20 m/s, revealing also the alterations in the rate of $\hat{z}_i$ changes with $\hat{t}$ under the effect of stronger shear.

To explain the observed differences in the CBL growth between sheared and shear-free CBL cases, one may invoke the following ZOM entrainment equation for sheared CBLs, which was proposed in Conzemius and Fedorovich (2006b) and which we use here for diagnostic purposes:

$$\frac{1}{B_s}\Delta b\frac{dz_i}{dt} = \frac{C_1}{1 - C_P Ri_{GS}^{-1}}, \tag{8}$$

where $C_1 = 0.2$, $C_P = 0.4$, and Ri_{GS} is the Richardson number associated with the entrainment-zone wind shear:

$$Ri_{GS} = \frac{\Delta b z_i}{(\Delta u^2 + \Delta v^2)}. \tag{9}$$

Equation (8) indicates that the entrainment flux ratio in the sheared CBL is highly dependent on the entrainment-zone shear. Note that, as discussed in Conzemius and Fedorovich (2006b), expression (8) has problems when $Ri_{GS} \leq 0.4$, predicting unrealistic values of entrainment ratio. Figure 5 shows the inverse of Richardson number, Ri_{GS}^{-1}, as a function of dimensionless time for the 27 simulated sheared CBLs. One can see that Ri_{GS}^{-1} is very small for all cases with $u_g = 5$ m/s, when the denominator of Equation 8 tends to 1, and the associated regime of entrainment is very close to that of the shear-free CBL. This supports the behaviour of the calculated $\hat{z}_i$ in Figure 4a. With the increasing of geostrophic wind, Ri_{GS}^{-1} becomes larger (see, e.g., Figure 5c), the denominator of Equation 8 decreases, and the entrainment rate increases significantly compared to the shear-free situation. Therefore, ZOM entrainment rates for CBL cases with greater geostrophic winds are expected to significantly depart from their counterparts for shear-free CBLs, as manifested in Figure 4c.

In addition to the analyses of entrainment rates, we compare entrainment regimes of the sheared CBL in terms of the actual entrainment ratio $A_i = -\delta Q_i/Q_s$. The corresponding data are shown in Figure 6. First, it should be noted that regardless of the magnitude of the geostrophic wind, A_i shows qualitatively the same tendencies that it exhibited with respect to changing N and Q_s in the shear-free case (section 3.1), that is, A_i increases with growing N and decreases with

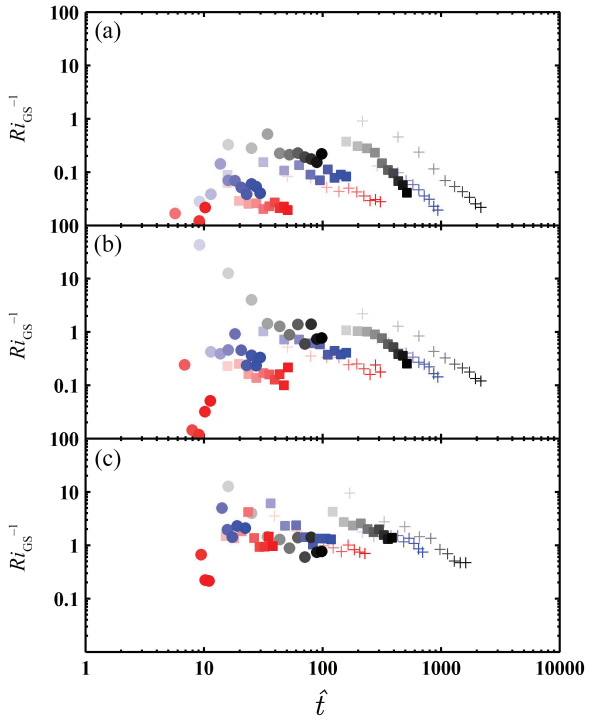

FIGURE 5 The inverse of Richardson number, $Ri_{GS}{}^{-1}$, as a function of dimensionless time for different geostrophic-wind magnitudes: (a) $u_g = 5$ m/s, (b) $u_g = 10$ m/s, and (c) $u_g = 20$ m/s. The symbols and colours are the same as in Figure 2 [Colour figure can be viewed at wileyonlinelibrary.com].

growing Q_s. Second, the entrainment flux ratio is substantially bumped up when geostrophic wind is strong (i.e. greater than 10 m/s). Third, the ratio is slightly reduced compared to its shear-free value when the geostrophic wind is weak (i.e. 5 m/s). Actually, Conzemius and Fedorovich (2006a), and Pino and Vilà-Guerau de Arellano (2008) also observed this slight reduction. They speculated this could be an effect of the so-called shear sheltering described in Hunt and Durbin (1999). Fourth, under conditions of strong geostrophic wind (Figure 6e–i), the entrainment flux ratio is rather large early in the simulation and decreases rapidly thereafter. Such evolution of A_i, which is totally different to its changes with time in the cases with weak geostrophic winds (Figure 6a–c) and shear-free entrainment (Figure 3), was also reported by Conzemius and Fedorovich (2006a), who proposed two reasons for these large initial values A_i with strong winds. Both are related to the shallowness of the CBL at the early stages of its development, which (a) causes strong entrainment-zone shear and associated enhancement of entrainment, and (b) is favourable for the vertical transport toward the entrainment zone of the TKE generated in the region of strong shear close to the surface.

In order to get more insights into the effect of shear on entrainment, we selected the simulated CBL case with the free-atmosphere temperature gradient $d\theta/dz = 0.01$ K/m and $Q_s = 0.03$ K m s^{-1} for a more detailed analysis. Some flow statistics for this case obtained by horizontal averaging with additional temporal averaging over the last 1,000 time steps (i.e. about 0.42–0.56 h), are presented in Figure 7. From u velocity component profile in Figure 7a one can trace relative distributions of velocity shear between the near-surface and entrainment-zone regions of the flow with different u_g. As indicated in Conzemius and Fedorovich (2006a), the entrainment-zone (elevated) shear plays the crucial role in

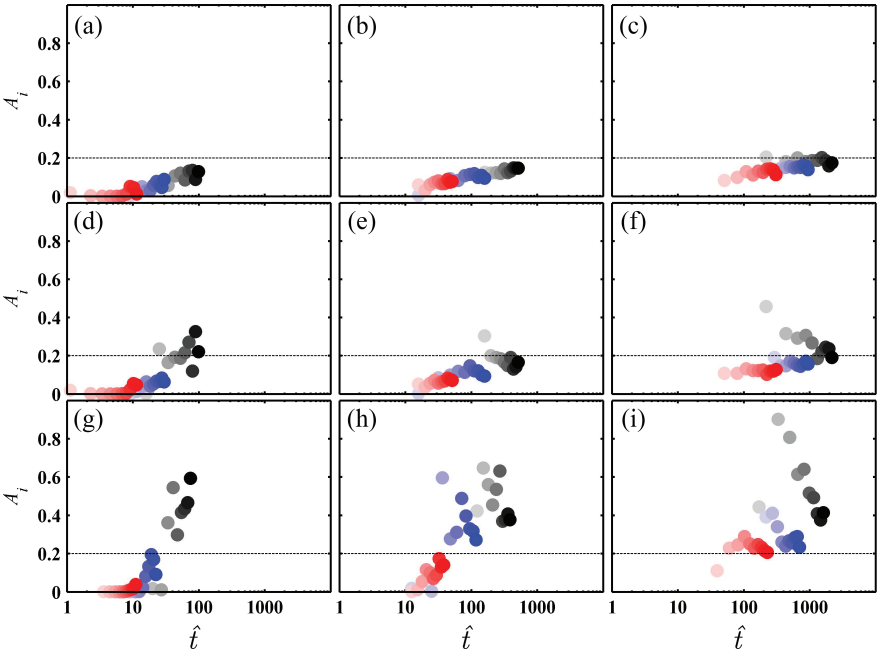

FIGURE 6 Entrainment flux ratio A_i as function of dimensionless time. Different rows represent different geostrophic-wind magnitudes, row 1, (a–c): $u_g = 5$ m/s; row 2, (d–f): $u_g = 10$ m/s; and row 3, (g–i): $u_g = 20$ m/s. Different columns denote different stratifications in the free atmosphere, column 1, (a,d,g): $d\theta/dz = 0.001$ K/m; column 2, (b,e,h): $d\theta/dz = 0.003$ K/m; and column 3, (c,f,i): $d\theta/dz = 0.01$ K/m. Symbols show LES data stratified over time: light colours indicate early times and dark colours indicate later times. Different colours correspond to different values of Q_s: black, $Q_s = 0.03$ K m s^{-1}; blue, $Q_s = 0.1$ K m s^{-1}; red, $Q_s = 0.3$ K m s^{-1} [Colour figure can be viewed at wileyonlinelibrary.com].

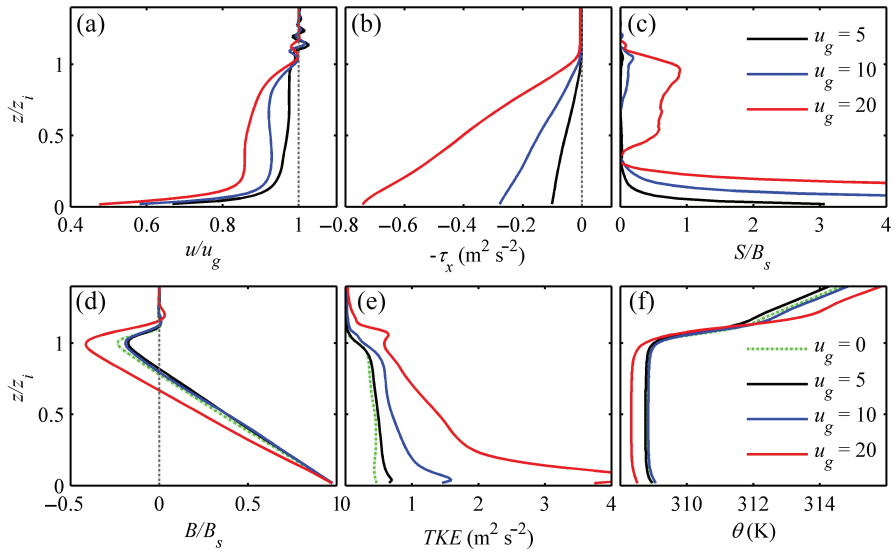

FIGURE 7 Profiles of the (a) x component of mean wind, (b) x component of kinematic momentum flux, (c) shear production rate of TKE, (d) buoyancy production rate of TKE, (e) TKE, and (f) potential temperature in the CBL with background $d\theta/dz = 0.01$ K/m and surface heat flux $Q_s = 0.03$ K m s^{-1} [Colour figure can be viewed at wileyonlinelibrary.com].

the enhancement of the entrainment process. In the case of the 5 m/s geostrophic wind, the velocity increment associated with this shear is practically unnoticeable, but it becomes increasingly strong with increasing u_g, and with $u_g = 20$ m/s it reaches about a quarter of the value of velocity increment across the near-surface portion of the flow. Corresponding changes of the x-component of kinematic momentum flux are illustrated in Figure 7b. The substantial increase of the momentum-flux magnitude in the upper portion of the layer leads to the growth of shear production of TKE in the entrainment region, shown by the S/B_s profiles for $u_g = 10$ m/s and 20 m/s in Figure 7c. This increased TKE production, primarily seen in the shear-production profile for $u_g = 20$ m/s, transforms into the stronger entrainment and greater entrainment ratio explicated by the larger magnitude of $B/B_s = Q/Q_s$ within the entrainment zone (Figure 7d). Inspection of the corresponding S/B_s profile for $u_g = 5$ m/s points to the relatively strong TKE production by surface shear and almost non-existent production by the elevated shear. Under such conditions, the surface shear apparently has a positive effect on the local turbulence production in the near-surface region, but at the same time it appears to impede transport of TKE from this region aloft, into the upper portion of the CBL, where this energy could contribute to the entrainment. One may hypothesize that the upward buoyancy-driven motions originating near the surface are tilted and incapacitated while crossing the sheared region and, as a result, become less effective in penetrating into the capping inversion region; this is also indicated by the TKE profiles (Figure 7e). The overall effect is the reduction of the entrainment ratio for $u_g = 5$ m/s as compared to the ratio for $u_g = 0$ (shear-free CBL), which may be interpreted as a particular form of the shear-sheltering. With $u_g = 10$ m/s, the combined effect of the surface and elevated shear on the entrainment is somewhere in-between: the surface shear still hampers transport of TKE upward, but the TKE production in the upper region of the CBL is sufficiently active to offset this effect. This places the entrainment-zone profile of B/B_s for $u_g = 10$ m/s in-between its counterparts for CBL cases with $u_g = 0$ and $u_g = 5$ m/s (Figure 7d). Although the shear-sheltering in the lower portion of the CBL with $u_g = 20$ m/s is even stronger than in the case with $u_g = 10$ m/s, this really does not matter for the entrainment, which is markedly enhanced (Figure 7d) in this case almost exclusively through the production of turbulence within the region of elevated shear. The entrainment zone with $u_g = 20$ m/s also becomes deeper than with weaker geostrophic winds, which is clearly explicated by the potential temperature profile (Figure 7f).

We further inspect the turbulence structure within the entrainment zone using snapshots of visualized potential temperature over vertical cross-sections of the LES domain shown in Figure 8. Under free-convection conditions (Figure 8a), the structure of the flow in the upper portion of the CBL is dominated by large-scale rising motions of relatively warm air (convective thermals), which maintain entrainment by penetration into the capping inversion layer, and compensating downward motions of the cooler air. These rising motions originating from the near-surface region of the flow appear to be noticeably handicapped in the case of $u_g = 5$ m/s (Figure 8b) under the alleged effect of the surface shear. In this case, only weak, small-scale structural features are observed in the vicinity of the capping inversion that conceivably are not capable of producing a noticeable entrainment effect. With a stronger geostrophic wind imposed, $u_g = 10$ m/s, the disturbances in the potential temperature pattern in the vicinity of the capping inversion reappear (Figure 8c), although now they reflect smaller-scale turbulent fluctuations characteristic of the shear-produced turbulence close to the CBL top. Amplitude and size of the disturbances further increase with

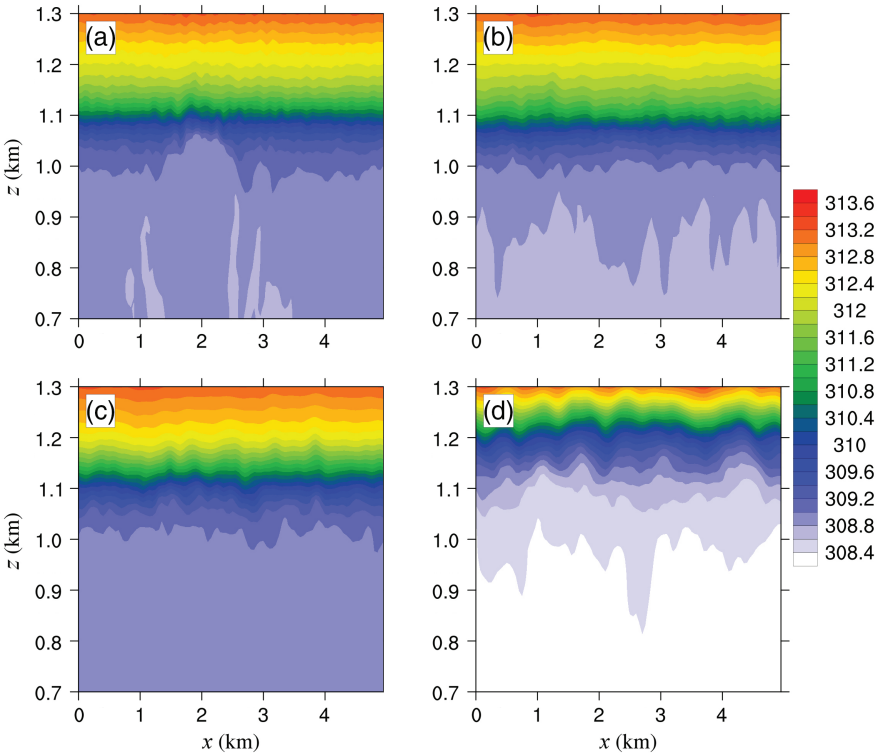

FIGURE 8 x–z cross-sections of the potential temperature field (K) averaged over last 1,000 time steps (i.e. about 0.42–0.56 h) with (a) no imposed wind, (b) $u_g = 5$ m/s, (c) $u_g = 10$ m/s, and (d) $u_g = 20$ m/s in the CBL with background $d\theta/dz = 0.01$ K/m and surface heat flux $Q_s = 0.03$ K m s^{-1}. Note that the time step is about 2.0 s for (a–c), and is about 1.5 s for (d), thus the actual simulation for different cases varies [Colour figure can be viewed at wileyonlinelibrary.com].

$u_g = 20$ m/s (Figure 8d), indicating potential of a stronger entrainment, while the entrainment zone becomes markedly deeper under the effect of active turbulence production by the elevated wind shear. This feature was observed in several previous studies of the sheared CBL (e.g. Kim *et al.*, 2003; Conzemius and Fedorovich, 2006a; Pino and Vilà-Guerau de Arellano, 2008).

The presented results point out the existence of two distinctive entrainment regimes in the sheared CBL with imposed height-constant unidirectional wind. The first regime is associated with weaker winds and results in the weakening of entrainment compared to shear-free CBL under the same thermal forcing conditions. It is characterized by the incapacitation, through erosion and tilting, of convective plumes rising from the surface by the wind shear concentrated in the lower portion of the layer, whilst the elevated shear remains undeveloped. In the second regime, when the imposed wind is sufficiently strong, the entrainment in sheared CBL is enhanced compared to the shear-free CBL. Such enhancement is a result of contribution of turbulent motions produced in the region of elevated shear, which develops in the upper region of the CBL under strong wind conditions. The above findings provide the answer to our question (2) from the Introduction.

3.3 | Free entrainment/encroachment

In previous sections we have addressed effects of the free-atmosphere potential temperature gradient on the entrainment. However, on some occasions, this gradient may be vanishingly small. The regime of CBL growth in the neutrally stratified atmosphere (with zero N) was referred to as "free entrainment" by Deardorff (1976) and, more correctly, as "free encroachment" (as there is no act of entrainment happening in this case, the entrainment flux is zero) by Sorbjan (1996). One may think of the CBL morning evolution, when the layer expands into a very weakly stratified residual layer from the previous day (Stull, 1998), as of the CBL growth regime closest to the free encroachment. Deardorff (1974) made a first estimate of the dimensionless entrainment rate $E = (dz_i/dt)/w_*$ in a regime of free encroachment from the evolution of a morning-time temperature profile and found it to be constant with a value about 0.2. Deardorff *et al.* (1980) further quantified this value in a laboratory-tank experiment and obtained an approximate constant value of $E = 0.24$. Zilitinkevich's (1991) ZOM theory also predicted constancy of E in the regime of free encroachment. Sorbjan (1996) used an extremely small temperature gradient (0.01 K/km) to reproduce the free encroachment in his LES, which yielded $E = 0.16$. More recently, Mellado (2012) reported a higher value of E (~0.4–0.5) from direct numerical simulation of CBL growing within a neutrally stratified fluid. The considerable scatter of E values from different studies should be primarily attributed to differences in definition and determination of z_i. For instance, Mellado (2012) determined z_i from the integral of buoyancy flux, while in the other studies a variety of methods based on threshold values of temperature and heat flux were used.

In order to revisit this issue, we conducted three LES experiments with $N = 0$ and three different values of the surface heat flux: 0.01, 0.03 and 0.1 K m s^{-1}. We diagnosed z_i using three methods: (a) from the elevation where the local heat flux reaches 1% of its surface value (hereinafter called the heat-flux method); (b) from the elevation where the difference between the mean potential temperature and reference potential temperature, $\theta - \theta_0$, reaches 1% of the difference between the surface temperature minus reference temperature, $\theta_s - \theta_0$, (hereinafter called the temperature method); (c) from the heat flux vertically integrated over the domain and divided by surface heat flux (hereinafter called the integral method, analogous to the one used in Mellado (2012)). Due to the fast growth of z_i with zero N, in the free-encroachment experiments we employed a larger domain of $X \times Y \times Z = 12\,\text{km} \times 12\,\text{km} \times 6\,\text{km}$ with a $600 \times 600 \times 300$ grid.

Figure 9 shows z_i as a function of time in the free-encroachment regime predicted by three methods with three different surface heat-flux values. After a transition, which takes different time for different Q_s, the CBL depths obtained by all three methods increase approximately linearly, with the heat-flux method predicting largest z_i, while the integral-method z_i estimates are the smallest. The dimensionless entrainment rates evaluated from these $z_i(t)$ data are shown in Figure 10. For all three methods and with all three Q_s values, E in the post-transition phase remains nearly constant with time. The heat-flux method provides overall highest E values within the interval from 0.6 to 0.7, while the integral-method estimates are the lowest, from 0.4 to 0.5, being rather close to the estimate of Mellado (2012). The temperature method yields E values in-between: from 0.5 to 0.6. The dependence of E on the method of z_i determination is thus stronger than on the heat-flux value. On the whole, all estimated E values exceed Deardorff's (1974; 1980) and Sorbjan's (1996) estimates, but our integral-method estimate shows consistency with the estimate of Mellado (2012) obtained from the same principles. Responding to our third question from the Introduction, we may state that dimensionless entrainment rate in the regime of free encroachment has a universal value independent of the surface heat flux.

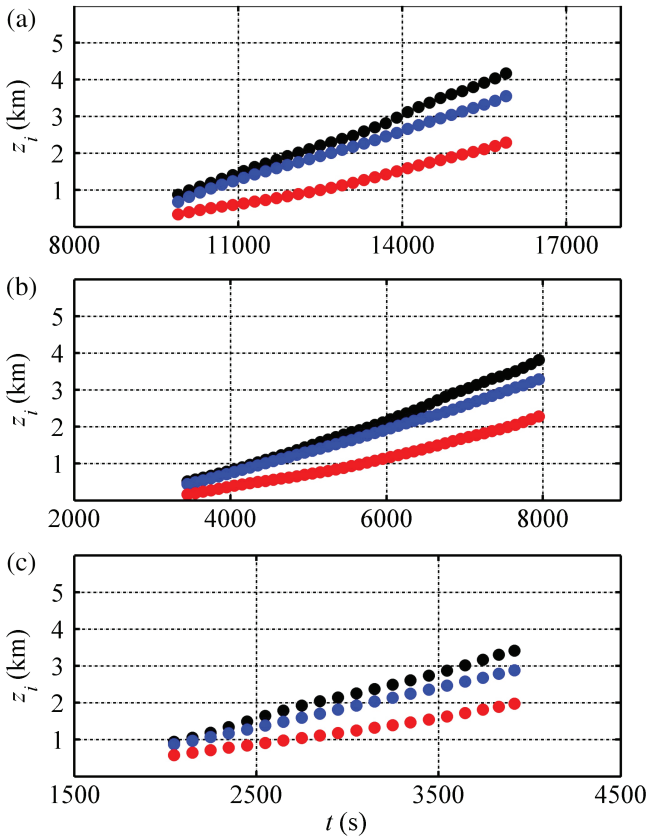

FIGURE 9 Evolution of z_i with different surface heat-flux values: (a) $Q_s = 0.01$ K m s^{-1}; (b) $Q_s = 0.03$ K m s^{-1}; and (c) $Q_s = 0.1$ K m s^{-1}. Different symbol colours indicate z_i diagnosed by different methods: heat-flux method (black); temperature method (blue); integral method (red) [Colour figure can be viewed at wileyonlinelibrary.com].

4 | SUMMARY AND CONCLUSIONS

In the reported study, LES has been employed to systematically investigate effects of diverse driving factors on the entrainment rate and entrainment flux ratio in shear-free and sheared CBL. Simulation results were evaluated and interpreted using a conceptual ZOM framework. It has been confirmed that ZOM entrainment flux ratio in the equilibrium shear-free CBL has a universal value ~0.2 regardless of the free-atmosphere stratification and the surface heat-flux value. In contrast to this, the actual entrainment flux ratio (directly evaluated from LES) is essentially stratification- and surface heat flux-dependent: it increases with growing N and decreases with growing Q_s. A physical reasoning has been offered to explain such dependence of the entrainment ratio on Q_s, which is complementary to the explanation of the dependence on N previously proposed in Fedorovich *et al.* (2004).

The impact of wind shear, associated with imposed unidirectional height-constant geostrophic winds of varying magnitude, on characteristics of the CBL entrainment has also been investigated by means of LES. It is commonly assumed, see, e.g., Conzemius and Fedorovich (2006a; 2006b) and review by Fedorovich and Conzemius (2008), that wind shear of any kind contributes to the enhancement of entrainment. We have found that entrainment flux ratio indeed significantly increases when geostrophic wind is strong (i.e. has a speed exceeding 10 m/s), but the entrainment ratio is slightly reduced under conditions of a weak geostrophic wind (having speed of 5 m/s in our case). In this case, thermal plumes rising from the surface are impeded by the wind shear in the near-surface layer in the absence of the elevated shear. When the imposed wind is sufficiently strong, the entrainment in sheared CBL is enhanced primarily due to the turbulence production in the region of elevated shear.

The CBL entrainment rate in the free-encroachment regime has been investigated with the focus on the effect of varying surface heat flux. It has been found that associated

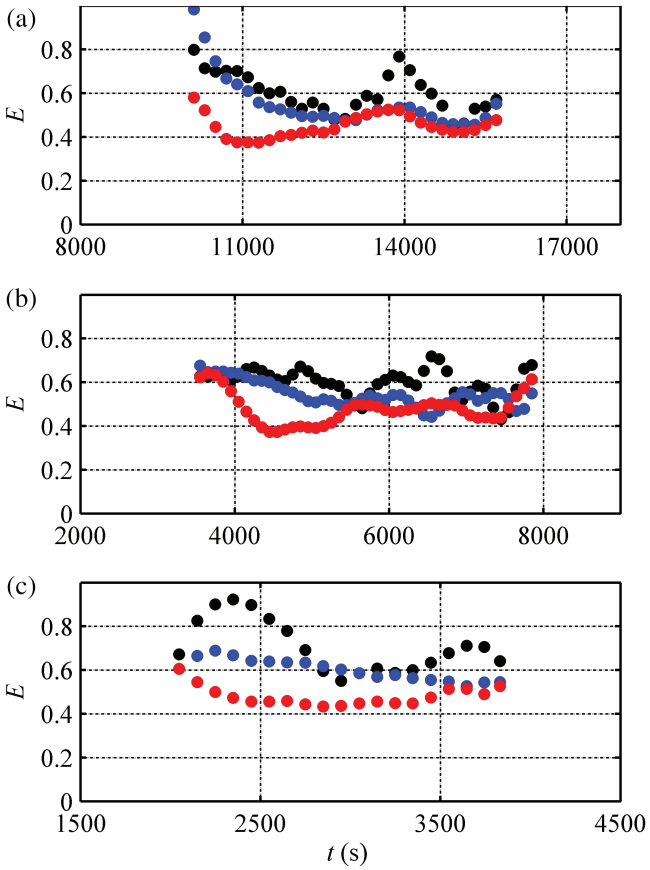

FIGURE 10 (a–c) Dimensionless entrainment rate E as function of time evaluated for three surface heat-flux values and using three determination methods. Notation is the same as in Figure 9 [Colour figure can be viewed at wileyonlinelibrary.com].

dimensionless entrainment rate E remains approximately constant and surface heat-flux independent, in agreement with previous estimates by Zilitinkevich (1991) and Mellado (2012), with the value in the range from 0.4 to 0.7, depending on the method of evaluation of the CBL depth from the LES data.

ACKNOWLEDGEMENTS

The research was supported jointly by the National Natural Science Foundation of China (Grant 41575009), the National Key Research and Development Program of China (2017YFC0210102), the Priority Academic Program Development of Jiangsu Higher Education Institutions (PAPD), and the Ministry of Education of China (Grant PCSIRT). The first author also acknowledges the support from Postgraduate Research and Practice Innovation Program of Jiangsu Province (Grant KYLX16_0945). This work was performed when the first author visited the School of Meteorology and Center for Analysis and Prediction of Storms (CAPS) of the University of Oklahoma (OU). The computing for this project was performed at the OU Supercomputing Center for Education and Research (OSCER) at the University of Oklahoma. The second author is grateful to Dmitrii Mironov for meaningful discussions regarding the physics of the investigated entrainment phenomena. We thank three anonymous reviewers for their suggestions, which greatly improve the manuscript.

ORCID

Cheng Liu https://orcid.org/0000-0002-5053-0208

REFERENCES

Angevine, W.M. (1999) Entrainment results including advection and case studies from the Flatland boundary layer experiments. *Journal of Geophysical Research*, 104(D24), 30947–30963.

Barr, A.G. and Strong, G.S. (1996) Estimating regional surface heat and moisture fluxes above prairie cropland from surface and upper-air measurements. *Journal of Applied Meteorology*, 35, 1716–1735.

Betts, A.K. (1973) Non-precipitating cumulus convection and its parameterization. *Quarterly Journal of the Royal Meteorological Society*, 99, 178–196.

Betts, A.K. (1974) Reply to comment on the paper "Non-precipitating cumulus convection and its parameterization". *Quarterly Journal of the Royal Meteorological Society*, 100, 469–471.

Betts, A.K. and Ball, J.H. (1994) Budget analysis of FIFE 1987 sonde data. *Journal of Geophysical Research*, 99(D2), 3655–3666.

Carson, D.J. (1973) The development of dry inversion-capped convectively unstable boundary layer. *Quarterly Journal of the Royal Meteorological Society*, 99, 450–467.

Conzemius, R. and Fedorovich, E. (2006a) Dynamics of sheared convective boundary layer entrainment. Part I: Methodological background and large-eddy simulations. *Journal of the Atmospheric Sciences*, 63, 1151–1178.

Conzemius, R. and Fedorovich, E. (2006b) Dynamics of sheared convective boundary layer entrainment. Part II: Evaluation of bulk model predictions of entrainment flux. *Journal of the Atmospheric Sciences*, 63, 1179–1199.

Conzemius, R. and Fedorovich, E. (2007) Bulk models of the sheared convective boundary layer: evaluation through large eddy simulations. *Journal of the Atmospheric Sciences*, 64, 786–807.

Deardorff, J.W. (1974) Three-dimensional numerical study of the height and mean structure of a heated planetary boundary layer. *Boundary-Layer Meteorology*, 7, 81–106.

Deardorff, J.W. (1976) On the entrainment rate of a stratocumulus-topped mixed layer. *Quarterly Journal of the Royal Meteorological Society*, 102, 563–582.

Deardorff, J.W. (1979) Prediction of convective mixed-layer entrainment for realistic capping inversion structure. *Journal of the Atmospheric Sciences*, 36, 424–436.

Deardorff, J.W. (1980) Stratocumulus-capped mixed layers derived from a three-dimensional model. *Boundary-Layer Meteorology*, 18, 495–527.

Deardorff, J.W., Willis, G.E. and Stockton, B.H. (1980) Laboratory studies of the entrainment zone of a convectively mixed layer. *Journal of Fluid Mechanics*, 100, 41–64.

Driedonks, A.G.M. (1982) Models and observations of the growth of the atmospheric boundary layer. *Boundary-Layer Meteorology*, 23, 283–306.

Driedonks, A.G.M. and Tennekes, H. (1984) Entrainment effects in the well-mixed atmospheric boundary layer. *Boundary-Layer Meteorology*, 30, 75–105.

Fedorovich, E. (1995) Modeling the atmospheric convective boundary layer within a zero-order jump approach: an extended theoretical framework. *Journal of Applied Meteorology*, 34, 1916–1928.

Fedorovich, E. and Mironov, D.V. (1995) A model for shear-free convective boundary layer with parameterized capping inversion structure. *Journal of the Atmospheric Sciences*, 52, 83–96.

Fedorovich, E. (1998) Bulk models of the atmospheric convective boundary layer. In: Plate, E.J., Fedorovich, E.E., Viegas, D.X. and Wyngaard, J.C. (Eds.) *Buoyant Convection in Geophysical Flows*. Dordrecht, Netherlands: Springer, pp. 265–290.

Fedorovich, E., Conzemius, R. and Mironov, D. (2004) Convective entrainment into a shear-free, linearly stratified atmosphere: bulk models re-evaluated through large eddy simulations. *Journal of the Atmospheric Sciences*, 61, 281–295.

Fedorovich, E. and Conzemius, R. (2008) Effects of wind shear on the atmospheric convective boundary layer structure and evolution. *Acta Geophysica*, 57, 114–141.

Garcia, J.R. and Mellado, J.P. (2014) The two-layer structure of the entrainment zone in the convective boundary layer. *Journal of the Atmospheric Sciences*, 71, 1935–1955.

Gibbs, J.A. and Fedorovich, E. (2014) Comparison of convective boundary layer velocity spectra retrieved from large-eddy-simulation and Weather Research and Forecasting model data. *Journal of Applied Meteorology and Climatology*, 53, 377–394.

Holtslag, A.A.M. and Duynkerke, P.G. (1998) *Clear and Cloudy Boundary Layers*. Amsterdam: Royal Netherlands Academy of Arts and Sciences.

Huang, J., Lee, X. and Patton, E.G. (2008) A modelling study of flux imbalance and the influence of entrainment in the convective boundary layer. *Boundary-Layer Meteorology*, 127, 273–292.

Huang, J., Lee, X. and Patton, E.G. (2009) Dissimilarity of scalar transport in the convective boundary layer in inhomogeneous landscapes. *Boundary-Layer Meteorology*, 130, 327–345.

Huang, J., Lee, X. and Patton, E.G. (2011) Entrainment and budgets of heat, water vapor, and carbon dioxide in a convective boundary layer driven by time-varying forcing. *Journal of Geophysical Research*, 116, D06308. https://doi.org/10.1029/2010JD014938.

Hunt, J.C.R. and Durbin, P.A. (1999) Perturbed vortical layers and shear sheltering. *Fluid Dynamics Research*, 24, 375–404.

Kim, S.W., Park, S.U. and Moeng, C.H. (2003) Entrainment processes in the convective boundary layer with varying wind shear. *Boundary-Layer Meteorology*, 108, 221–245.

Kim, S.W., Park, S.U., Pino, D. and Vilà-Guerau de Arellano, J. (2006) Parameterization of entrainment in a sheared convective boundary layer using a first-order jump model. *Boundary-Layer Meteorology*, 120, 455–475.

Klemp, J.B. and Durran, D.R. (1983) An upper boundary condition permitting internal gravity wave radiation in numerical mesoscale models. *Monthly Weather Review*, 111, 430–444.

Lilly, D.K. (1968) Models of cloud-topped mixed layers under a strong inversion. *Quarterly Journal of the Royal Meteorological Society*, 94, 292–309.

Lilly, D.K. (2002) Entrainment into mixed layers. Part I: Sharp-edged and smoothed tops. *Journal of the Atmospheric Sciences*, 59, 3340–3352.

Mellado, J.P. (2012) Direct numerical simulation of free convection over a heated plate. *Journal of Fluid Mechanics*, 712, 418–450.

Moeng, C.H. (1984) A large-eddy-simulation model for the study of planetary boundary-layer turbulence. *Journal of the Atmospheric Sciences*, 41, 2052–2062.

Moeng, C.H. and Sullivan, P.P. (1994) A comparison of shear-and buoyancy-driven planetary boundary layer flows. *Journal of the Atmospheric Sciences*, 51, 999–1022.

Patton, E.G., Sullivan, P.P. and Moeng, C.H. (2005) The influence of idealized heterogeneity on wet and dry planetary boundary layers coupled to the land surface. *Journal of the Atmospheric Sciences*, 62, 2078–2097.

Pino, D., Vilà-Guerau de Arellano, J. and Duynkerke, P.G. (2003) The contribution of shear to the evolution of a convective boundary layer. *Journal of the Atmospheric Sciences*, 60, 1913–1926.

Pino, D., Vilà-Guerau de Arellano, J. and Kim, S.W. (2006) Representing sheared convective boundary layer by zeroth- and first-order-jump mixed-layer models: large-eddy simulation verification. *Journal of Applied Meteorology and Climatology*, 45, 1224–1243.

Pino, D. and Vilà-Guerau de Arellano, J. (2008) Effects of shear in the convective boundary layer: analysis of the turbulent kinetic energy budget. *Acta Geophysica*, 56, 167–193.

Salesky, S.T., Chamecki, M. and Bou-Zeid, E. (2017) On the nature of the transition between roll and cellular organization in the convective boundary layer. *Boundary-Layer Meteorology*, 163, 41–68.

Sorbjan, Z. (1996) Effects caused by varying the strength of the capping inversion based on a large eddy simulation model of the shear-free convective boundary layer. *Journal of the Atmospheric Sciences*, 53, 2015–2024.

Stull, R.B. (1973) Inversion rise model based on penetrative convection. *Journal of the Atmospheric Sciences*, 30, 1092–1099.

Stull, R.B. (1976) The energetics of entrainment across a density interface. *Journal of the Atmospheric Sciences*, 33, 1260–1267.

Stull, R.B. (1998) *An Introduction to Boundary Layer Meteorology*. Dordrecht, Netherlands: Kluwer Academic.

Sullivan, P.P., McWilliams, J.C. and Moeng, C.H. (1994) A subgrid-scale model for large-eddy simulation of planetary boundary-layer flows. *Boundary-Layer Meteorology*, 71, 247–276.

Sullivan, P.P., McWilliams, J.C. and Moeng, C.H. (1996) A grid nesting method for large-eddy simulation of planetary boundary-layer flows. *Boundary-Layer Meteorology*, 80, 167–202.

Sun, J. and Wang, Y. (2008) Effect of the entrainment flux ratio on the relationship between entrainment rate and convective Richardson number. *Boundary-Layer Meteorology*, 126, 237–247.

Tennekes, H. (1973) A model for the dynamics of the inversion above a convective boundary layer. *Journal of the Atmospheric Sciences*, 30, 558–567.

Van Zanten, M.C., Duynkerke, P.G. and Cuijpers, J.W.M. (1999) Entrainment parameterization in convective boundary layers. *Journal of the Atmospheric Sciences*, 56, 813–828.

Zeman, O. and Tennekes, H. (1977) Parameterization of the turbulent energy budget at the top of the daytime atmospheric boundary layer. *Journal of the Atmospheric Sciences*, 34, 111–123.

Zilitinkevich, S.S. (1991) *Turbulent Penetrative Convection*. Aldershot, UK: Avebury Press.

How to cite this article: Liu C, Fedorovich E, Huang J. Revisiting entrainment relationships for shear-free and sheared convective boundary layers through large-eddy simulations. *Q J R Meteorol Soc.* 2018;144:2182–2195. https://doi.org/10.1002/qj.3330